Research Square

Preprints are preliminary reports that have not undergone peer review.
They should not be considered conclusive, used to inform clinical practice,
or referenced by the media as validated information.

Biosynthesis-Integrated Editing of Bacterial Cellulose Enables Sequence-Programmable Biointerfaces

Guang Yang

gyang-hust@hust.edu.cn

Huazhong University of Science and Technology

Guoliang Tang

Huazhong University of Science and Technology

Qi He

Fudan University

Shidong Zou

Huazhong University of Science and Technology

Hao Wang

Huazhong University of Science and Technology

Guobin Huang

Tongji Hospital, Tongji Medical College, Huazhong University of Science and Technology

Wenqi Yin

Huazhong University of Science and Technology

Zhijun Shi

Huazhong University of Science and Technology

Zhishui Chen

Tongji Hospital, Tongji Medical College, Huazhong University of Science and Technology

https://orcid.org/0000-0003-3803-5682

Lin Yin

Fudan University

Guosong Chen

Fudan University https://orcid.org/0000-0001-7089-911X

Article

Keywords:

Posted Date: November 6th, 2026

DOI: https://doi.org/10.21203/rs.3.rs-11476274/v1

License: This work is licensed under a Creative Commons Attribution 4.0 International License.
Read Full License

Additional Declarations: There is **NO** Competing Interest.

Abstract

Structural polysaccharides self-assemble into densely packed fibrils, providing a molecular foundation for the hierarchical organization and mechanical integrity of biological materials. However, the same interchain interactions that stabilize these structures severely restrict chemical accessibility, making molecular editing after assembly a formidable challenge. Here, we integrate regiochemical editing into bacterial cellulose biosynthesis using azido-glucose analogues substituted at C2, C3, or C6. The resulting cellulose materials exhibit regioisomer-dependent differences in crystallinity, fibrillar organization, and mechanical properties, while precursor feeding further modulates crystallinity. The incorporated azide groups remain chemically accessible after assembly, enabling DNA conjugation and rolling-circle amplification to construct sequence-programmable aptamer interfaces. By varying the aptamer sequence, the same cellulose platform can be reprogrammed for either selective cell capture and release or HGF-mimetic regulation of endothelial behavior. This work establishes a biosynthesis-integrated strategy that connects molecular editing during cellulose formation with hierarchical material organization and subsequent biological programming.

INTRODUCTION

Structural polysaccharides serve as load-bearing components of biological materials, such as cell walls and arthropod exoskeletons, through the ordered association of carbohydrate chains into crystalline fibrils and higher-order architectures[1–4]. These densely packed assemblies, however, substantially restrict the accessibility of reactive sites, particularly those buried within crystalline domains[2,5]. Cellulose illustrates this molecular constraint (Fig. 1a). Its abundant hydroxyl groups provide potential sites for covalent modification but also participate in the intra- and intermolecular hydrogen bonds that support the assembly of glucan chains during biosynthesis[6,7]. Once established, extensive hydrogen bonding and dense chain packing make molecular editing particularly difficult without disrupting the assembled structure[8,9].

Efforts to address this challenge have included two complementary approaches. Top-down cellulose chemistry introduces functionalities into preformed materials, providing control over their chemical and physical properties, but such modification generally occurs after crystallization and hierarchical assembly have already been established (Fig. 1b)[10,11]. Achieving more extensive modification can require harsh chemical treatments that risk disrupting cellulose crystallinity, compromising mechanical integrity, or even causing chain degradation[12]. Bottom-up approaches, including automated glycan assembly[13,14], enzyme-catalyzed oligosaccharide synthesis[15,16], and ring-opening polymerization[17,18], provide complementary control over glucan covalent structures. Iterative glycan synthesis often involves repeated protection and coupling steps, yielding defined cellulose that can form nanomaterials (Fig. 1c). These approaches operate outside the cellulose-forming process, making it difficult to examine how such modifications influence its hierarchical structure.

Bacterial cellulose (BC) biosynthesis offers a way to introduce molecular modifications before its hierarchical structure is fully established[19–23]. During this process, glucan chains are synthesized and assembled into fibrils, linking molecular synthesis to higher-order organization. Previous studies have demonstrated that modified glucose precursors, including azide, amino- and fluorophore-bearing glucose derivatives, can be used to functionalize BC during its formation[19,23–25]. However, how the regiochemistry of these precursors relates to the hierarchical organization of cellulose remains poorly understood. Given the distinct roles of C2, C3, and C6 hydroxyl groups in cellulose hydrogen bonding[6,26], we reasoned that regioisomeric glucose analogues bearing the same azide functionality could provide a way to investigate this relationship, while also examining whether the introduced groups remain chemically accessible after assembly.

Here, we establish such a biosynthesis-integrated regiochemical editing strategy by incorporating C2-, C3-, and C6-substituted azido-glucose analogues during BC formation. The resulting materials retain the native cellulose I crystalline polymorph while exhibiting regioisomer-dependent differences in crystallinity, fibrillar organization, and mechanical properties (Fig. 1d). The introduced azide groups remain chemically accessible after assembly, enabling bioorthogonal DNA conjugation and in situ rolling-circle amplification (RCA) to construct sequence-programmable aptamer interfaces. Aptamer sequence selection provides a simple way to redirect the biological function of the same BC scaffold toward either selective capture and release of EpCAM-positive cells or HGF-mimetic regulation of endothelial behavior. This work demonstrates how molecular editing during polysaccharide biosynthesis can connect precursor-level chemical design with the hierarchical organization while retaining chemical handles for subsequent functional programming. This concept may open new opportunities for engineering structural polysaccharides at the molecular level as their hierarchical architectures are formed, enabling new approaches to the design of functional biological materials.

RESULTS AND DISCUSSION

Regioisomeric Molecular Editing during Cellulose Biosynthesis. To test whether BC biosynthesis could accommodate structurally modified glucose substrates, *K. sucrofermentans* was cultured with 2-, 3-, or 6-azido-glucose (2-, 3-, or 6-N_3-Glc), yielding the corresponding 2-, 3-, and 6-N_3-BC variants (Fig. 2a). These analogues differ in the position of the azide functionality, providing a set of defined molecular perturbations. Raman spectra of all three N_3-BC variants exhibited a characteristic azide-stretching band in the 2100–2140 cm^{-1} region, absent from native BC (Fig. 2b), while Fourier transform infrared spectroscopy (FTIR) showed the corresponding absorption at approximately 2140 cm^{-1} (**Fig. S1**). Confocal Raman mapping further detected azide-associated signals along the cellulose fibers of all three variants (Fig. 2c), supporting the presence of azide functionality within the biosynthesized material. X-ray photoelectron spectroscopy (XPS) provided complementary evidence for the chemical identity of the azide groups. The N 1s spectra contained lower-binding-energy components at approximately 399–401 eV together with a distinct high-binding-energy component near 405 eV, consistent with the chemically nonequivalent nitrogen atoms of an organic azide (Fig. 2d)[27]. Solid-state ^{13}C nuclear

magnetic resonance (ss^{13}C NMR) further revealed regioisomer-dependent differences in the local chemical environment of the glucan chains relative to native BC (**Fig. S2-S5**). Together, these complementary spectroscopic results support the biosynthetic incorporation of azide-bearing glucose analogues into BC, with distinct local glucan-chain environments associated with the different precursor regioisomers.

We next examined whether the incorporated azide groups remained chemically accessible after assembly. Treatment of 2-N_3-BC with DBCO–Cy3 produced intense fluorescence along the cellulose fibers (Fig. 2e), whereas native BC subjected to the same labeling conditions exhibited negligible fluorescence (**Fig. S6**), consistent with labeling of accessible azide groups through strain-promoted azide–alkyne cycloaddition (SPAAC). Moreover, the normalized Cy3 fluorescence increased with increasing 2-N_3-Glc concentration in the culture feed and approached a plateau at 5–10 mM (Fig. 2e), suggesting that precursor feeding influences the availability of chemically accessible azide groups in the resulting BC. These results support the retention of reactive azide functionalities after cellulose assembly and demonstrate that the post-assembly labeling response can be modulated through precursor feeding.

Structural and Mechanical Consequences of Regioisomeric Editing. X-ray diffraction (XRD) analysis showed that all N_3-BC variants retained the characteristic reflections of cellulose I, indicating preservation of the native crystalline polymorph (Fig. 3a). However, the diffraction peak intensities varied with precursor regioisomer, with more pronounced attenuation observed for 2-N_3-BC and 3-N_3-BC than for 6-N_3-BC. Quantitative analysis showed that crystallinity decreased from 83.3% for native BC to 70.9% for 6-N_3-BC, 66.8% for 2-N_3-BC, and 64.9% for 3-N_3-BC. Crystalline organization was also sensitive to precursor composition: increasing the 3-N_3-Glc fraction in the feed progressively attenuated the cellulose I reflections and reduced crystallinity from approximately 79% at 1% feed to approximately 36% at 100% feed. These results suggest that cellulose crystalline organization can be modulated by both precursor regiochemistry and the proportion of modified glucose supplied during biosynthesis.

The effects of molecular editing were also reflected in the fibrillar and network organization of the resulting cellulose. Scanning electron microscopy (SEM) revealed pronounced differences in both surface and cross-sectional morphology among the native BC and N_3-BC variants (Fig. 3b). Native BC exhibited a relatively dense surface network and an organized, lamellar fibrillar structure in cross-section, whereas 2-N_3-BC and 3-N_3-BC displayed more open surface networks and less ordered cross-sectional architectures. In contrast, 6-N_3-BC retained a fibrillar organization more similar to that of native BC. These morphological differences paralleled the changes in crystallinity observed by XRD.

These structural differences were further reflected in the macroscopic mechanical properties of the materials (Fig. 3c). The fracture strength decreased to 1.55 MPa for 2-N_3-BC and 1.39 MPa for 3-N_3-BC, whereas 6-N_3-BC retained a higher value of 2.60 MPa. All three edited N_3-BC variants exhibited greater strain at break than native BC, with 3-N_3-BC showing the largest increase. Thus, the greater structural

changes observed for 2-N_3-BC and 3-N_3-BC were accompanied by lower fracture strength and increased deformability. These mechanical changes are consistent with the altered crystalline organization and fibrillar architectures observed in the edited materials. The N_3-BC variants also demonstrated good biocompatibility comparable to that of native BC, with favorable cytocompatibility and low hemolytic activity confirmed by CCK-8, live/dead staining, and hemolysis assays (**Fig. S7–S9**).

DNA Functionalization after Cellulose Assembly. The azide functionality retained in biosynthetically modified BC was subsequently used to construct a sequence-defined DNA interface. Using 2-N_3-BC as a representative scaffold, a DBCO-modified ssDNA primer was annealed to an aptamer-encoding ssDNA template, followed by ligation to form a circular DNA template. The resulting circular primer-template complex was then conjugated to 2-N_3-BC through SPAAC, followed by rolling circle amplification (RCA) from the immobilized primer (Fig. 4a). This approach combines bioorthogonal DNA immobilization with enzymatic amplification directly on the preassembled cellulose scaffold. The kinetics of SPAAC conjugation were monitored by surface-enhanced Raman spectroscopy (SERS). Upon addition of the DBCO-modified DNA complex, the integrated intensity of the azide-stretching band near 2140 cm^{-1} decreased rapidly, falling to less than 10% of its initial value within 10 min (Fig. 4b). This rapid decrease is consistent with the consumption of accessible azide groups during SPAAC. The immobilized primer subsequently supported RCA, with DNA amplification increasing over 8 h (**Fig. S10**), supporting the continued accessibility of the surface-bound DNA to polymerase-mediated extension. The loading of RCA products on the scaffold was further examined. The DNA loading concentration increased with increasing DNA input, whereas loading efficiency decreased at higher concentrations, consistent with a progressive occupation of accessible coupling sites (Fig. 4c).

The resulting DNA aptamer-functionalized BC (Apt-N_3-BC) was characterized by fluorescence imaging and Raman spectroscopy. Gel-Green staining of BC pellicles revealed strong fluorescence from Apt-N_3-BC, compared with the much weaker signal from native BC (Fig. 4d), supporting the presence of DNA on the modified cellulose scaffold. Fluorescence microscopy revealed DNA-associated fluorescence along the cellulose structures, with normalized fluorescence increasing with DNA input before approaching a plateau (Fig. 4e). Raman spectroscopy showed vibrational features assigned to nucleobase-associated C = O/C = N region, while confocal Raman mapping localized these signals along the cellulose fibers (Fig. 4f). The spectroscopic and fluorescence results support the conversion of biosynthetically introduced azide groups into a DNA-functionalized interface through SPAAC and subsequent RCA, establishing a route to sequence-programmable functionalization after cellulose assembly.

Sequence-Defined Cell Capture and Release. To determine whether the sequence-defined DNA interface could be translated into a specific biological output, we first programmed the scaffold with an epithelial cell adhesion molecule (EpCAM)-targeting aptamer (Aptamer1) for selective capture of EpCAM-positive cells (Fig. 5a)[28]. Before evaluating capture on the BC scaffold, we examined the binding specificity of the free Aptamer1. Fluorescence imaging showed colocalization between EpCAM immunostaining and the FAM-labeled Aptamer1 at the 4T1 cell membrane (Fig. 5b), while flow cytometry confirmed sequence-

dependent binding, with markedly higher fluorescence on EpCAM-positive 4T1 cells than on EpCAM-negative HUVECs or reverse-Aptamer1-sequence controls (**Fig. S11**). The apparent K_d was 49.9 ± 7.3 nM (**Fig. S12**), supporting high-affinity binding of the Aptamer1 to EpCAM-positive cells. We then assessed capture performance directly on the Aptamer1-functionalized BC (Apt1-N_3-BC) scaffold. In a mixed-cell system containing approximately equal numbers of 4T1 cells and HUVECs, Apt1-N_3-BC selectively retained 4T1 cells while washing removed most HUVECs, resulting in a 4T1 fraction of 98.5% among the captured cells (Fig. 5c). Capture assays performed separately with each cell type further quantified this selectivity. Apt1-N_3-BC captured more than 800 4T1 cells mm^{-2} but fewer than 10 HUVECs mm^{-2}, whereas native BC and reverse-aptamer-sequence-functionalized BC (Rev-N_3-BC) showed minimal nonspecific adhesion (Fig. 5d). These controls support the role of aptamer sequence-specific recognition in cell capture, rather than nonspecific adhesion to the cellulose scaffold. Capture reached a plateau within 25 min of incubation, while capture performance increased with RCA reaction time and approached saturation after approximately 7 h, consistent with a contribution from the amplified aptamer layer to cell capture (**Fig. S13-S14**).

We next examined whether captured cells could be released by enzymatic degradation of the DNA layer[29–31]. The enzymatically cleavable DNA interface offers a route to recover captured cells by removing the recognition layer rather than disrupting the underlying cellulose scaffold. Single-cell fluorescence imaging showed a DiI-labeled 4T1 cell surrounded by the Gel-Green-stained DNA network before treatment (Fig. 5e). Following DNase I exposure, the DNA-associated fluorescence disappeared while the labeled cell remained intact (Fig. 5f), consistent with enzymatic disruption of the DNA network. DNase I treatment released 62% of the captured cells within 30 min and 73% within 60 min (**Fig. S15**). The released cells retained their morphology and adhered and spread after 24 h of culture. Live/dead staining further showed a post-release viability of 98.6%. These findings demonstrate that the aptamer-programmed BC interface combines selective enrichment of target cells with enzyme-triggered release, allowing the captured cells to be recovered with high viability.

Sequence-Dependent Regulation of Endothelial Behavior. We next examined whether changing the aptamer sequence could redirect the biological function of the same biosynthetically edited BC scaffold. The immobilized aptamer was replaced with a Met-targeting agonistic sequence (Aptamer2) previously reported to exhibit HGF-mimetic activity (Fig. 6a)[32,33]. To compare presentation modes, both monovalent Aptamer2-functionalized BC (Apt2-N_3-BC) and multivalent RCA-N_3-BC were prepared. HUVECs were selected as the model system because HGF/Met signaling is known to regulate endothelial proliferation, migration, and morphogenesis[34,35]. Cell–material interactions were first evaluated by directly seeding HUVECs onto the materials. Cytoskeletal staining showed that cells on Apt2-N_3-BC and RCA-N_3-BC displayed organized actin networks and intact nuclei, with cell coverage reaching 86.7% on RCA-N_3-BC, compared with 75.6% on Apt2-N_3-BC, 34.2% on native BC, and 34.6% on Rev-N_3-BC (Fig. 6b). Calcein-AM/PI staining on Day 5 further showed cell viability of 95.5% on Apt2-N_3-BC, compared with 89.5% on native BC and 89.9% on Rev-N_3-BC. RCA-N_3-BC further increased cell density (173 cells mm^{-2}) relative to

Apt2-N_3-BC (137 cells mm^{-2}) (**Fig. S16**). To further evaluate endothelial responses, HUVECs were cultured with material extracts and their metabolic activity was assessed by CCK-8 assay over 6 days. Apt2-N_3-BC and RCA-N_3-BC both increased HUVEC metabolic activity to more than 200% of the BC control, whereas Rev-N_3-BC remained comparable to control (Fig. 6c). Metabolic activity increased with the input concentration of the monovalent aptamer, and RCA-N_3-BC produced the strongest response in this assay, consistent with an enhanced effect at higher local aptamer density.

The effects of Aptamer2-functionalized BC on endothelial migration and morphogenesis were further evaluated. Wound-scratch assays revealed that Apt2-N_3-BC, RCA-N_3-BC, and HGF all accelerated wound closure to approximately 90%, significantly above the 75% closure observed with native BC, while Rev-N_3-BC showed no significant effect (Fig. 6d **and Fig. S17**). Under these conditions, monovalent and multivalent presentation produced comparable wound-healing responses. A Geltrex tube-formation assay further showed that Apt2-N_3-BC, RCA-N_3-BC, and HGF all promoted interconnected capillary-mimetic networks, increasing branch points to more than 200% and total tube length to approximately 150% of the BC control (Fig. 6e **and Fig. S18**). Rev-N_3-BC again showed no significant effect, and no statistical difference was observed between monovalent and multivalent presentation or between the aptamer-functionalized groups and HGF treatment. Together, these results show that aptamer sequence selection allows a common biosynthetically edited BC scaffold to support distinct biological functions, from selective cell capture to HGF-mimetic regulation of endothelial behavior, without changing the underlying cellulose chemistry.

CONCLUSION

In summary, we established biosynthesis-integrated molecular editing of bacterial cellulose by introducing C2-, C3-, and C6-substituted azido glucose regioisomers during cellulose formation. The resulting materials retained the native cellulose I polymorph while exhibiting regioisomer-dependent differences in crystallinity, fibrillar organization, and mechanical properties, with precursor feed composition providing an additional way to modulate crystallinity. The incorporated azide groups remained chemically accessible after assembly, enabling bioorthogonal DNA conjugation and in situ rolling circle amplification to generate sequence-programmable aptamer interfaces. By selecting different aptamer sequences, the same BC scaffold could be programmed for selective EpCAM-positive cell capture and nuclease-mediated release or HGF-mimetic regulation of endothelial behavior. Demonstrating this strategy in cellulose, whose densely packed fibrils restrict post-assembly chemical modification, highlights biosynthesis as a tool for molecular editing. More broadly, this approach may extend to other polysaccharides whose biosynthetic machinery accommodates modified sugar precursors, offering opportunities to modulate their structures during formation and retain chemical handles for subsequent functional programming.

DECLARATIONS

ACKNOWLEDGEMENTS

This work was supported by the National Key Research and Development Program of China (Grant No. 2025YFE0120100), the National Natural Science Foundation of China (Grant No. 52373235, 52573322, 82371794, and 82572043) and Hubei Provincial Science and Technology Program Project (Grant No. 2025BCB012). Dr. Lin Yin thanks the National Natural Science Foundation of China (Grant No. 22601078) and the China Postdoctoral Science Foundation (Grant No. 2026M791005) for financial support. The authors are grateful to the Analytical and Testing Centre and Core Facilities of Life Sciences of Huazhong University of Science and Technology for providing scientific research instruments. The authors also thank Prof. Pingchuan Sun and Dr. Zeming Feng for their valuable discussions and technical assistance.

SUPPORTING INFORMATION

Additional experimental procedures and characterization details are provided in the Supplementary Information.

DATA AVAILABILITY

The data supporting the findings of this study are available within the Article and its Supplementary Information. Additional data are available from the corresponding authors upon reasonable request.

AUTHOR CONTRIBUTIONS

G.Y. and G.T. conceptualized and administered the project. G.T. and L.Y. wrote the paper. G.T. and Q.H. performed the cellulose biosynthesis editing, aptamer functionalization and mechanistic studies, analysed the data and prepared the figures. Q.H. and L.Y. assisted in azido-glucose analogues synthesis and supported characterization experiments. S.Z., H.W., and G.H. assisted in cell experiments. W.Y., Z.S., Z.C., and G.C. contributed to data interpretation and assisted in revising the paper. Z.C., L.Y., G.C., and G.Y. analysed and interpreted the results and contributed to paper revision.

REFERENCES

1. Ling S, Kaplan DL, Buehler MJ (2018) Nanofibrils in nature and materials engineering. Nat Rev Mater 3:18016
2. Tardy BL et al (2021) Deconstruction and reassembly of renewable polymers and biocolloids into next generation structured materials. Chem Rev 121:14088–14188
3. Bai L et al (2022) Nanochitin: chemistry, structure, assembly, and applications. Chem Rev 122:11604–11674
4. Wegst UGK, Bai H, Saiz E, Tomsia AP, Ritchie RO (2015) Bioinspired structural materials. Nat Mater 14:23–36

5. Heise K et al (2022) Spatioselective surface chemistry for the production of functional and chemically anisotropic nanocellulose colloids. J Mater Chem A 10:23413–23432
6. Nishiyama Y, Langan P, Chanzy H (2002) Crystal structure and hydrogen-bonding system in cellulose Iβ from synchrotron X-ray and neutron fiber diffraction. J Am Chem Soc 124:9074–9082
7. Fittolani G, Vargová D, Seeberger PH, Ogawa Y, Delbianco M (2022) Bottom-up approach to understand chirality transfer across scales in cellulose assemblies. J Am Chem Soc 144:12469–12475
8. Verdía Barbará P et al (2025) Recent advances in the use of ionic liquids and deep eutectic solvents for lignocellulosic biorefineries and biobased chemical and material production. Chem Rev 125:5461–5583
9. Xu L, Mao Y, Hu L (2026) Molecular engineering of cellulose and its applications. Nat Rev Bioeng 4:490–502
10. Fatona A, Berry RM, Brook MA, Moran-Mirabal JM (2018) Versatile surface modification of cellulose fibers and cellulose nanocrystals through modular triazinyl chemistry. Chem Mater 30:2424–2435
11. Beaumont M et al (2021) Unique reactivity of nanoporous cellulosic materials mediated by surface-confined water. Nat Commun 12:2513
12. Ge W, Shuai J, Wang Y, Zhou Y, Wang X (2022) Progress on chemical modification of cellulose in green solvents. Polym Chem 13:359–372
13. Guberman M, Seeberger PH (2019) Automated glycan assembly: a perspective. J Am Chem Soc 141:5581–5592
14. Plante OJ, Palmacci ER, Seeberger PH (2001) Automated solid-phase synthesis of oligosaccharides. Science 291:1523–1527
15. Kuga T et al (2026) Enzyme-directed assembly of antiparallel cellulose II nanocrystals: unraveling the mechanism beyond spontaneous crystallization. JACS Au 6:154–165
16. Kobayashi S, Kashiwa K, Kawasaki T, Shoda S (1991) -i. Novel method for polysaccharide synthesis using an enzyme: the first in vitro synthesis of cellulose via a nonbiosynthetic path utilizing cellulase as catalyst. J Am Chem Soc 113:3079–3084
17. Nakatsubo F, Kamitakahara H, Hori M (1996) Cationic ring-opening polymerization of 3,6-di-*O*-benzyl-α-D-glucose 1,2,4-orthopivalate and the first chemical synthesis of cellulose. J Am Chem Soc 118:1677–1681
18. Wu L et al (2024) Precision cellulose from living cationic polymerization of glucose 1,2,4-orthopivalates. J Am Chem Soc 146:7963–7970
19. Gao M et al (2019) A natural in situ fabrication method of functional bacterial cellulose using a microorganism. Nat Commun 10:437
20. Liu X et al (2022) Direct synthesis of photosensitizable bacterial cellulose as engineered living material for skin wound repair. Adv Mater 34:2109010

21. Morgan JLW, Strumillo J, Zimmer J (2012) Crystallographic snapshot of cellulose synthesis and membrane translocation. Nature 493:181–186
22. Saadi MASR et al (2025) Flow-induced 2D nanomaterials intercalated aligned bacterial cellulose. Nat Commun 16:5825
23. Chen S et al (2026) Bio-orthogonal functionalization of bacterial cellulose combining metabolic glycoengineering and click chemistry. Nat Commun 17:2304
24. Yin S et al (2024) Advanced composite solid electrolyte architecture constructed with amino-modified cellulose and carbon nitride via biosynthetic avenue. Adv Funct Mater 34:2314976
25. Sun Y et al (2025) Microbe-assisted fabrication of circularly polarized luminescent bacterial cellulosic hybrids. Nat Commun 16:1115
26. Nishiyama Y, Sugiyama J, Chanzy H, Langan P (2003) Crystal structure and hydrogen bonding system in cellulose Iα from synchrotron X-ray and neutron fiber diffraction. J Am Chem Soc 125:14300–14306
27. Zorn G et al (2014) X–ray photoelectron spectroscopy investigation of the nitrogen species in photoactive perfluorophenylazide-modified surfaces. J Phys Chem C 118:376–383
28. Song Y et al (2013) Selection of DNA aptamers against epithelial cell adhesion molecule for cancer cell imaging and circulating tumor cell capture. Anal Chem 85:4141–4149
29. Zhao W et al (2012) Bioinspired multivalent DNA network for capture and release of cells. *Proc. Natl. Acad. Sci. USA* 109, 19626–19631
30. Song Y et al (2019) Bioinspired engineering of a multivalent aptamer-functionalized nanointerface to enhance the capture and release of circulating tumor cells. Angew Chem Int Ed 58:2236–2240
31. Lin Y et al (2019) DNA-mediated reversible capture and release of circulating tumor cells with a multivalent dual-specific aptamer coating network. Chem Commun 55:5387–5390
32. Ueki R, Ueki A, Kanda N, Sando S (2016) Oligonucleotide-based mimetics of hepatocyte growth factor. Angew Chem Int Ed 55:579–582
33. Ueki R et al (2020) A chemically unmodified agonistic DNA with growth factor functionality for in vivo therapeutic application. Sci Adv 6:eaay2801
34. Zhang Y-W, Su YL, Volpert OV, Van de Woude GF (2003) Hepatocyte growth factor/scatter factor mediates angiogenesis through positive VEGF and negative thrombospondin 1 regulation. *Proc. Natl. Acad. Sci. USA* 100, 12718–12723
35. Xin X et al (2001) Hepatocyte growth factor enhances vascular endothelial growth factor-induced angiogenesis in vitro and in vivo. Am J Pathol 158:1111–1120

Figures

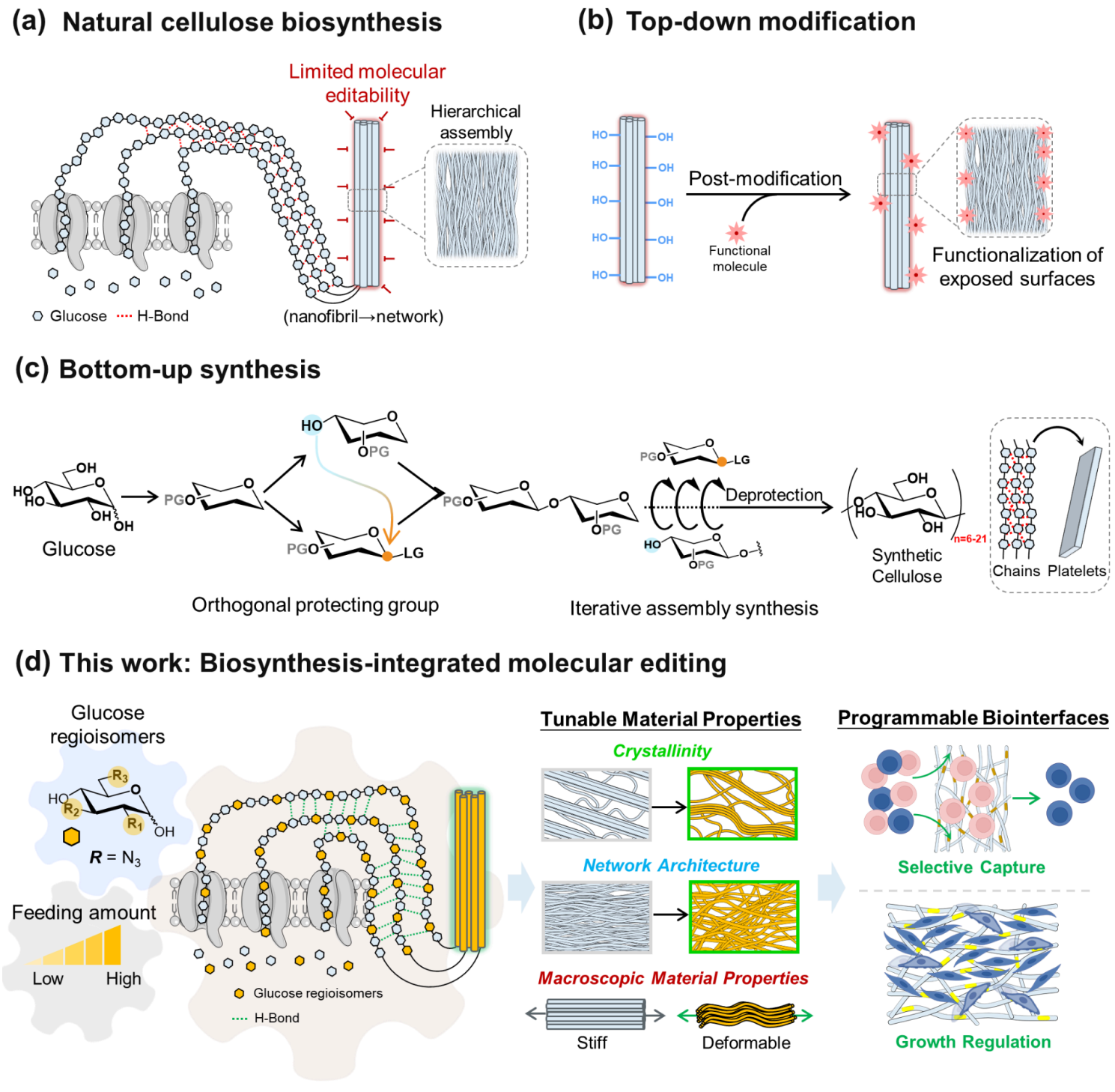


Figure 1

Conventional cellulose modification strategies and biosynthesis-integrated molecular editing. a, Natural cellulose biosynthesis, in which newly synthesized cellulose chains assemble into densely packed fibrillar networks, resulting in limited molecular editability after assembly. **b,** Top-down modification of preassembled cellulose, primarily introducing functional groups onto exposed surfaces with limited access to the densely packed interior. **c,** Representative bottom-up synthesis of short cellulose chains through iterative glycosylation and deprotection (PG, protecting group; LG, leaving

group), followed by their assembly into platelets, as illustrated in the inset. **d,** Biosynthesis-integrated regiochemical editing using C2-, C3-, and C6-substituted azido-glucose analogues at varying feeding levels, yielding cellulose materials with regioisomer-dependent differences in crystallinity, fibrillar organization, and macroscopic mechanical properties. The retained azide groups further enable DNA conjugation and subsequent rolling-circle amplification to construct sequence-programmable aptamer interfaces for selective cell capture and endothelial growth regulation.

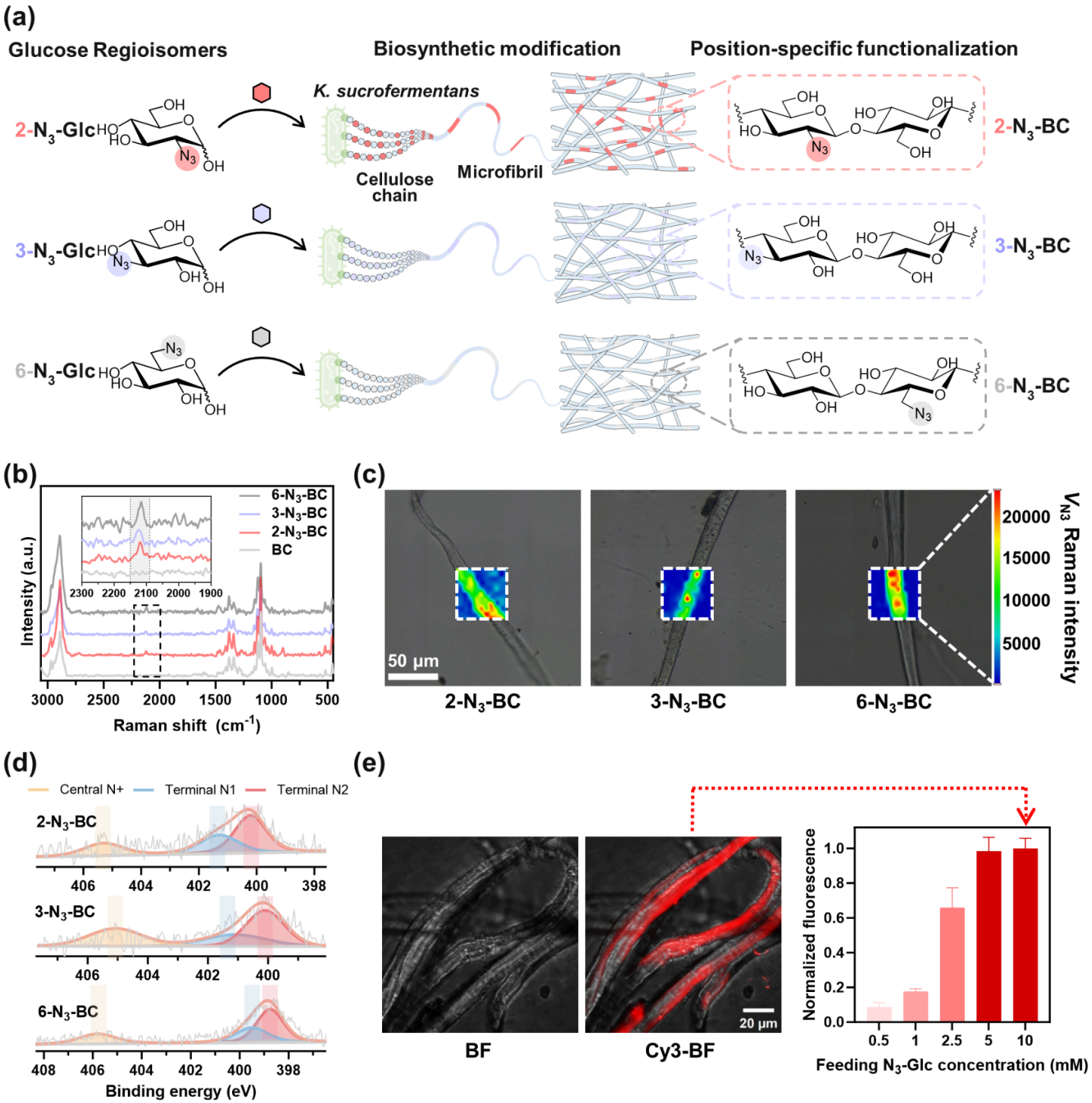


Figure 2

Regioisomeric molecular editing during cellulose biosynthesis. a, Schematic illustration of the biosynthetic incorporation of C2-, C3-, and C6-N_3-Glc regioisomers into BC by *K. sucrofermentans* yielding the corresponding 2-, 3-, and 6-N_3-BC variants. **b,** Raman spectra of native BC and N_3-BC variants; inset shows the azide-stretching region. **c,** Confocal Raman maps of the azide-stretching intensity, showing the spatial distribution of azide functionalities in N_3-BC variants. Mapping area: 50 × 50 μm. **d,** N 1s XPS spectra of N_3-BC variants with peak deconvolution. The high-binding-energy component at ~405 eV is assigned to the electron-deficient central nitrogen of the azide group, whereas the lower-binding-energy components at ~399–401 eV arise predominantly from the remaining azide nitrogen atoms. **e,** Representative bright-field (BF) and fluorescence micrographs of 2-N_3-BC after conjugation with DBCO–Cy3 (red) through SPAAC, and corresponding normalized Cy3 fluorescence intensities as a function of the 2-N_3-Glc feeding concentration (0.5–10 mM). Fluorescence intensities were normalized to the value obtained at 10 mM (set to 1). Scale bar, 20 μm. Error bars represent standard deviations (SD).

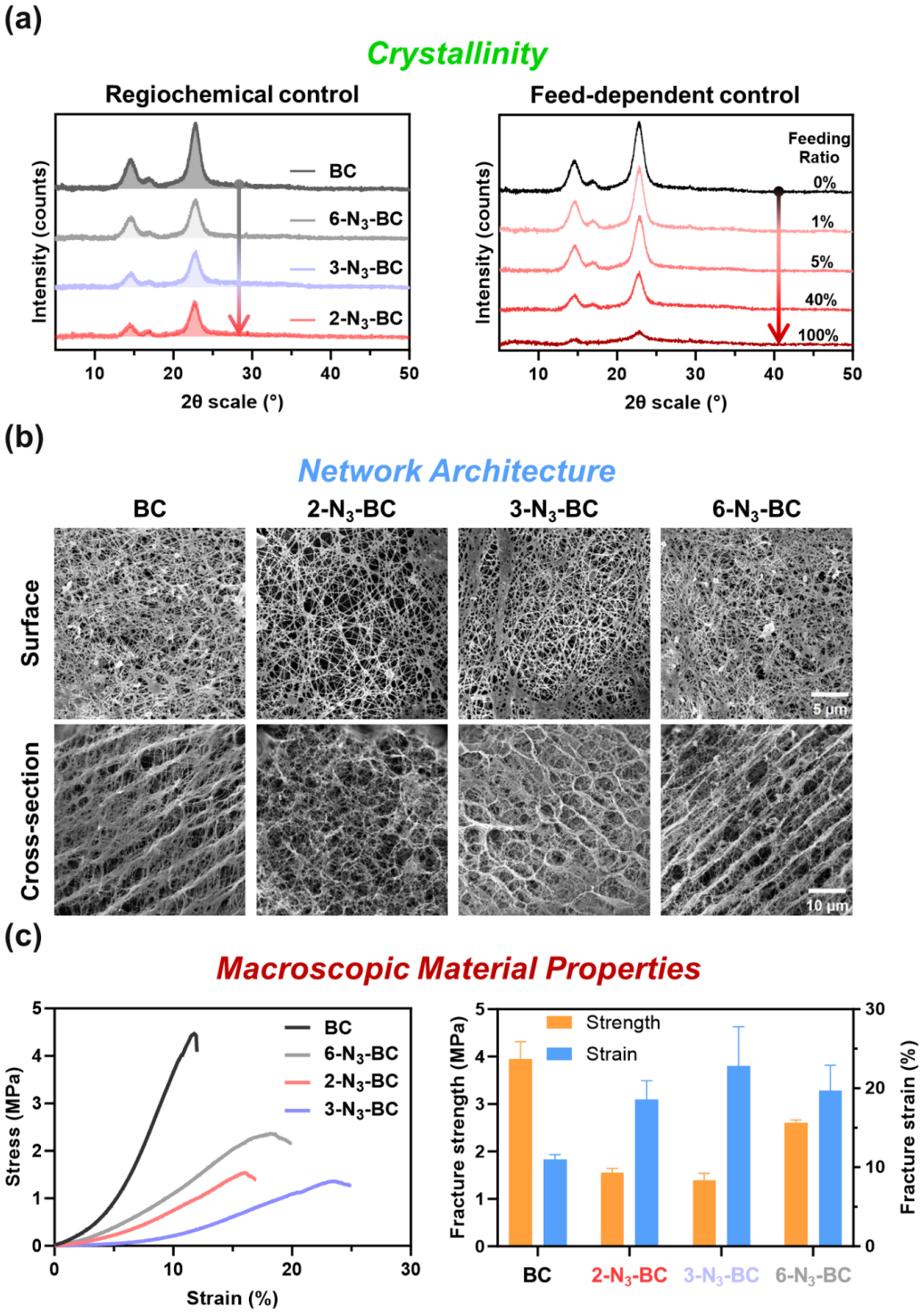


Figure 3

Propagation of molecular perturbations across cellulose hierarchy. a, XRD patterns of native BC and N_3-BC variants (left), and 3-N_3-BC prepared with varying N_3-Glc feeding fractions (right). **b,** Representative SEM images showing the surface and cross-sectional morphologies of native BC and N_3-BC variants. Scale bars, 5 μm (surface) and 10 μm (cross-section). **c,** Representative tensile stress–strain curves (left) and corresponding fracture strengths and strains at break (right) of native BC and N_3-BC variants. Error bars represent SD.

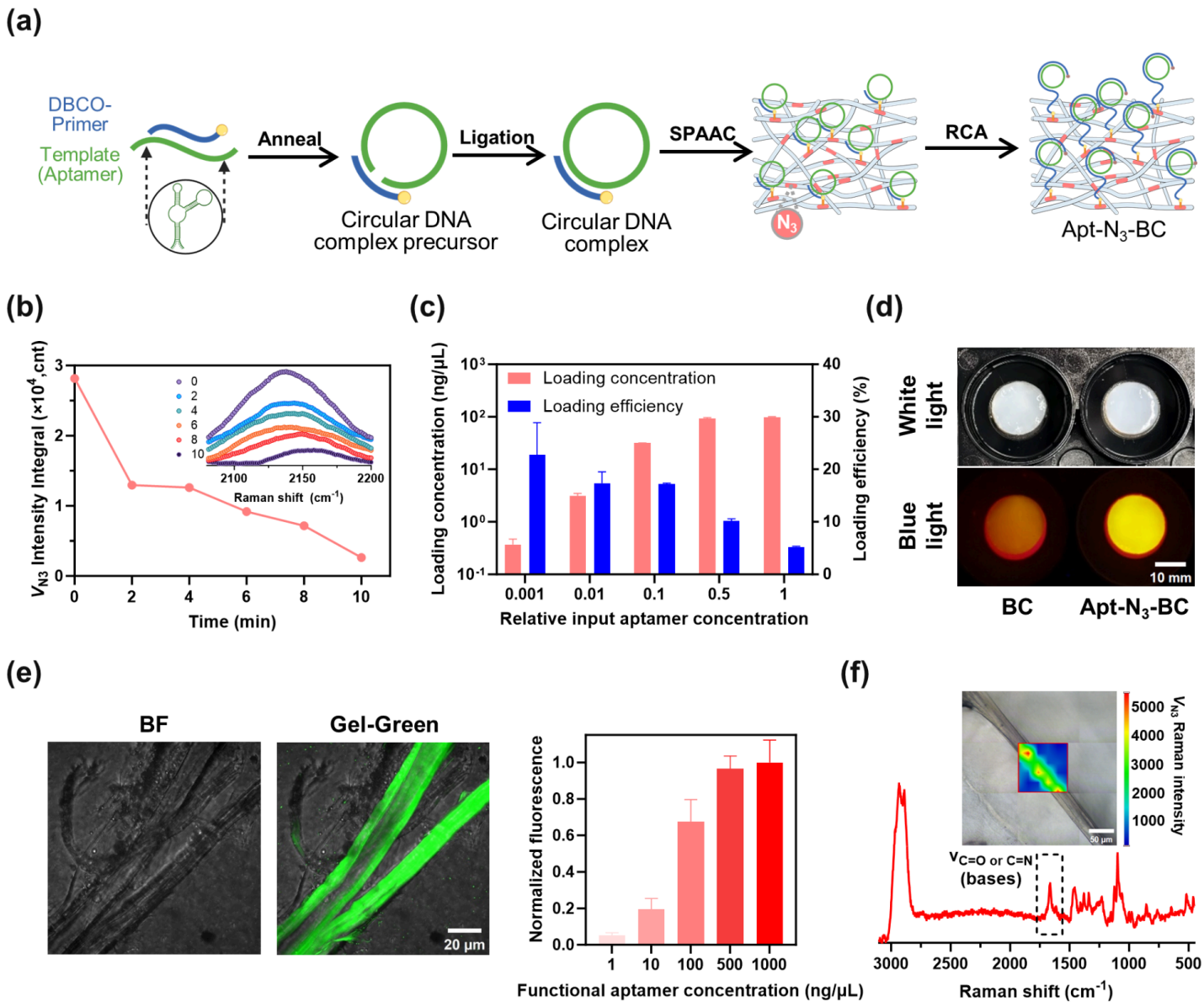


Figure 4

Chemical addressability after cellulose assembly. a, Schematic illustration of the preparation of Apt-N_3-BC through formation of a circular DNA template, immobilization of the DBCO-modified primer-template complex onto 2-N_3-BC via SPAAC, and subsequent RCA. **b,** Time-dependent integrated intensity of the azide-stretching band in N_3-BC monitored after addition of the DBCO-modified DNA complex, showing attenuation of the azide signal consistent with its consumption during SPAAC. The inset shows the corresponding Raman spectra in the azide-stretching region. **c,** DNA loading concentration and loading efficiency on N_3-BC as a function of the relative input aptamer concentration, normalized to the maximum concentration of RCA products obtained after 8 h of amplification. **d,** Photographs of BC and Apt-N_3-BC pellicles stained with Gel-Green (DNA-binding dye, green fluorescence) under white light and blue-light excitation. Scale bar, 10 mm. **e,** Representative bright-field and Gel-Green fluorescence micrographs of Apt-N_3-BC, together with the normalized fluorescence intensity at different functional

aptamer concentrations. Fluorescence intensities were normalized to the maximum value at 1000 ng/μL. Scale bar, 20 μm. **f,** Raman spectrum of Apt-N_3-BC and confocal Raman map showing the spatial distribution of nucleobase-associated vibrational signals (C=O/C=N) on the cellulose fibers. Mapping area: 100 × 100 μm. Error bars represent SD.

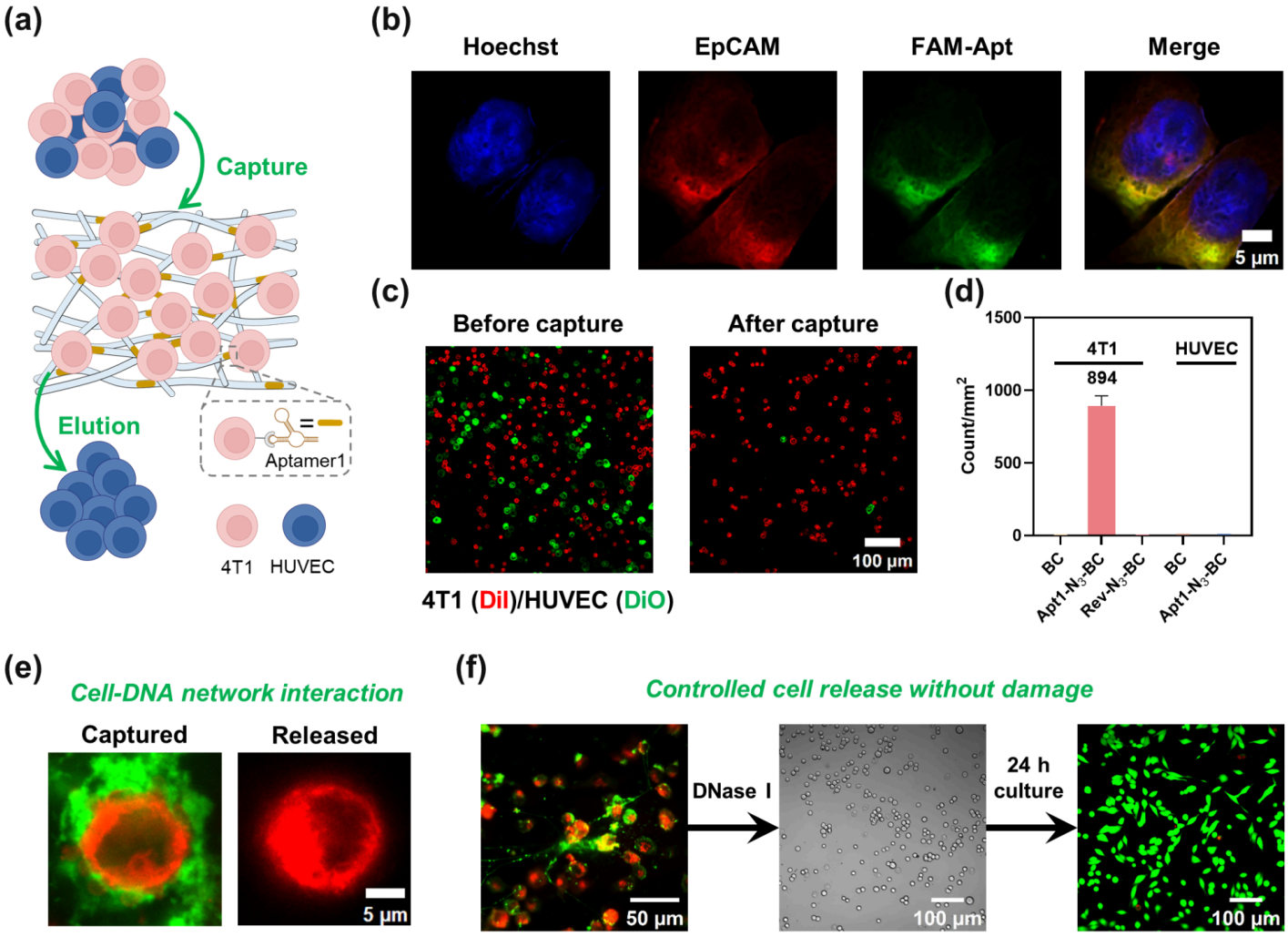


Figure 5

Sequence-defined cell capture and release. a, Schematic of EpCAM-targeting Apt1-N_3-BC for selective cell capture from a heterogeneous population. The inset illustrates the interaction between Aptamer1 and cell-surface EpCAM. **b,** Fluorescence images of 4T1 cells showing Hoechst-stained nuclei (blue), EpCAM immunostaining (red), and FAM-labeled aptamer (green). Scale bar, 5 μm. **c,** Selective capture from a mixture of CM-DiI (cell membrane-binding dye, red)-labeled 4T1 cells and CM-DiO (cell membrane-binding dye, green)-labeled HUVECs. Images show the cell population before capture and after capture and washing. Scale bar, 100 μm. **d,** Quantification of 4T1 cell and HUVEC capture densities on native BC, Apt1-N_3-BC, and Rev-N_3-BC. **e,** Single-cell fluorescence images before and after DNase I treatment, with the cell membrane labeled by CM-DiI and the aptamer network stained by Gel-Green. Scale bars, 5 μm. **f,** DNase I-triggered release of captured 4T1 cells. The Gel-Green-stained aptamer

network surrounding CM-DiI-labeled cells was degraded by DNase I, and the morphology and viability of released cells were assessed by bright-field imaging and live/dead staining (live, green; dead, red). Scale bars, 50 μm (left) and 100 μm (middle and right). Error bars represent SD.

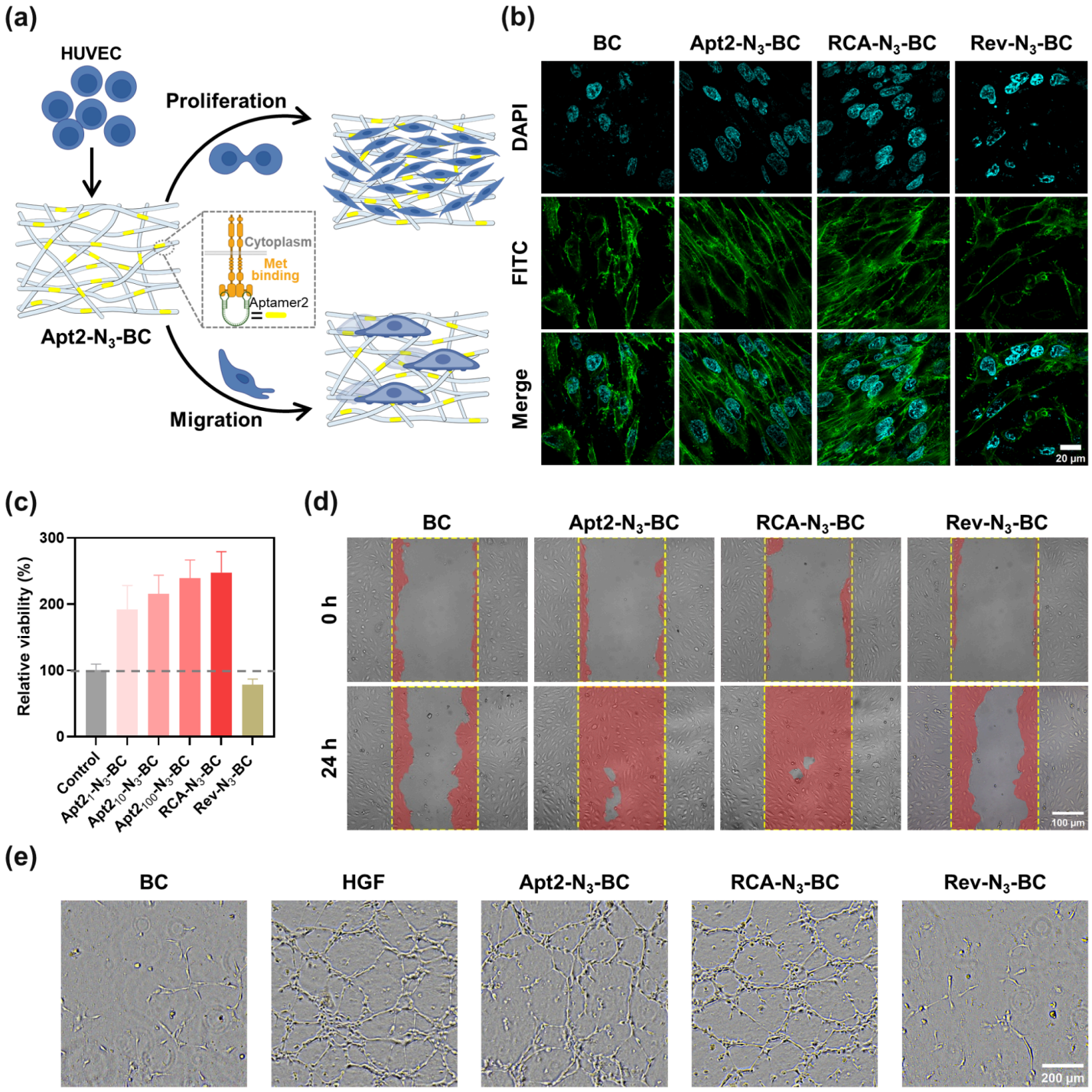


Figure 6

Sequence-dependent reprogramming of endothelial behavior. a, Schematic of Met-targeting Aptamer2-functionalized BC as an HGF-mimetic interface for modulating endothelial behavior. **b,** Representative fluorescence images of HUVECs cultured on native BC, Apt2-N_3-BC, RCA-N_3-BC, and Rev-N_3-BC. F-actin

and nuclei were stained with FITC-phalloidin (green) and DAPI (blue), respectively. Scale bar, 20 μm. **c,** HUVEC metabolic activity over 6 days assessed by CCK-8 assay after culture with extracts of native BC, Apt2-N_3-BC prepared using different monovalent aptamer input concentrations of 1, 10, 100 nM ($Apt2_1$-N_3-BC, $Apt2_{10}$-N_3-BC, and $Apt2_{100}$-N_3-BC), RCA-N_3-BC, and Rev-N_3-BC. **d,** Scratch-wound migration assay of HUVECs cultured with extracts of native BC, Apt2-N_3-BC, RCA-N_3-BC, or Rev-N_3-BC, with representative images acquired at 0 and 24 h. Scale bar, 100 μm. **e,** HUVEC tube formation on Geltrex, showing representative capillary-like networks. Scale bar, 100 μm. Error bars represent SD.

Supplementary Files

This is a list of supplementary files associated with this preprint. Click to download.

- Supplementaryinformation.docx